Chemical Pressure Maps of Molecules and Materials: Merging the Visual and Physical in Bonding Analysis

Hussien H. Osman,[†,§] Miguel A. Salvadó,[†] Pilar Pertierra,[†] Joshua Engelkemier,[‡] Daniel C. Fredrickson,[‡,*] and J. Manuel Recio[†,‡,*]

[†]MALTA-Consolider Team and Departamento de Química Física y Analítica, Universidad de Oviedo, E-33006, Oviedo, Spain

[§]Department of Chemistry, Faculty of Science, Helwan University, Ain-Helwan, 11795, Cairo, Egypt

[‡]Department of Chemistry, University of Wisconsin-Madison, 1101 University Avenue, Madison, Wisconsin 53706, United States

ABSTRACT: The characterization of bonding interactions in molecules and materials is one of the major applications of quantum mechanical calculations. Numerous schemes have been devised to identify and visualize chemical bonds, including the electron localization function, quantum theory of atoms in molecules, and natural bond orbital analysis, whereas the energetics of bond formation are generally analyzed in qualitative terms through various forms of energy partitioning schemes. In this article, we illustrate how the Chemical Pressure (CP) approach recently developed for analyzing atomic size effects in solid state compounds provides a basis for merging these two approaches, in which bonds are revealed through the forces of attraction and repulsion acting between the atoms. Using a series of model systems that include simple molecules (H_2, CO_2, and S_8), extended structures (graphene and diamond), systems exhibiting intermolecular interactions (ice and graphite), as well as simple representatives of metallic and ionic bonding (Na and NaH, respectively), we show how CP maps can differentiate a range of bonding phenomena. The approach also allows for the partitioning of the potential and kinetic contributions to the interatomic interactions, yielding schemes that capture the physical model for the chemical bond offered by Ruedenberg and coworkers.

INTRODUCTION

While the chemical bond has an undeniable reality to chemists, established by a wealth of empirical data, it has long been an elusive and controversial concept from the point of view of quantum mechanics.[1] Part of this difficulty arises from the fact that a bond's presence is not directly observable in itself, but is instead inferred indirectly from interatomic distances, bond enthalpies, and electron density maps. To fill this gap between chemical experience and theory, a number of approaches have been developed to analyze bonding in the results of quantum mechanical calculations. These have generally focused on (1) identifying signatures of bonding in the wavefunctions,[2-12] density matrices,[13-19] electron density,[20,21] or some derivative function,[22-28] or (2) decomposing the energy of an interaction in physically meaningful terms.[29-31] The insights afforded by these approaches pursued separately and in combination are immense, forming the subject of numerous reviews and monographs.[32-37] And yet, even recently the physical nature of the attractive forces within a chemical bond has been the subject of debate,[38-41] suggesting that important information may being lost between the spatial features of the former and the integrated energetic values of the latter. In this article, we will see how these two approaches can be merged in the recently developed chemical pressure (CP) method, yielding schemes in which balance of attractive and repulsive forces within chemical bonds are visually apparent.[42]

The two approaches to analyzing bonding mentioned above can be largely understood as considering different aspects of the solution to Schrödinger's equation for a system: the wavefunctions and the energy eigenvalues. The wavefunctions, and the electron densi-

ty distribution they underlie, have served as a basis for a range of methods for analyzing bonds with two major philosophies.[43] In the first school of thought, the chemical objects are searched for in orbital space. For example, the use of localized molecular orbitals,[2,3] Wannier functions,[4-8] or Natural Bond Orbitals[13-19] transforms the wavefunctions of a system into functions corresponding to chemically meaningful entities, such as bonds and lone pairs. Meanwhile, the second basic school focuses on orbital-invariant observables, typically scalars constructed from reduced density matrices either in real or momentum space, leading to a range of approaches that can be grouped under the term quantum chemical topology (QCT).[44] A plethora of scalar (and vector) fields have been analyzed, including the electron density itself (as in Bader's quantum theory of atoms in molecules),[18] kinetic energy densities,[45] the Electron Localization Function and Indicator (ELF and ELI),[22-28] and many others.[35,36]

The energies obtained from quantum mechanical calculations have also inspired the development of analytical tools. The total energies calculated for a compound can be partitioned in a variety of ways.[29-31] Some of these are perturbative in nature, and make use of reference states, such as the symmetry adapted perturbation theory (SAPT)[46] and the extended transition state-natural orbitals for chemical valence (ETS-NOCV)[47] incarnation of ideas originating with Morokuma.[47] In all these methods, the influence of the reference state may be large, motivating some alternatives which use QCT partitionings to provide an intrinsic energy decomposition. The interacting quantum atoms approach (IQA) belongs to this class.[48]

The issue of reference states is in fact one of the central points of contention in the characterization of the physical origin of the chemical bond. One of the most fruitful of the energy partitioning approaches to understanding the covalent bond was pioneered by Ruedenberg in the 1960s, with an analysis of how the separate kinetic and potential energy contributions lead to the cohesion between atoms in a covalent system.[49-51] In these studies, a compelling story emerged based on the classic conflict between the potential energy's drive to localize electrons around the atomic nuclei, and the kinetic energy costs of localization: the ability of electrons to delocalize over a pair of atoms in a bond lowers the kinetic energy penalty to concentrating the electrons near the nuclei. These conclusions have since been reaffirmed by other authors and increasingly accurate calculations,[39,40,52-55] however its use of linear combinations of the free-atom atomic orbitals as reference states has raised the objections of those adhering to the earlier view that electrostatic attraction between the nuclei and the internuclear electron density provides the basis of the covalent bond.[41]

In this article, we will demonstrate that the physical insights of Ruedenberg's model can be obtained in a virtually reference-free fashion, while capturing the graphical aspects of such approaches as the ELF, using the chemical pressure (CP) method, a simple formulation of the quantum mechanical stress density[56-60] that has emerged in the context of solid state chemistry.[42] In this approach, the macroscopic pressure obtained from a density functional theory (DFT) calculation on a compound is spatially resolved into local, interatomic components, which reflect forces calling for the expansion and contraction of the structure.

So far, this approach has mainly been applied to explaining structural phenomena—structural transformations in intermetallic compounds,[61] complex structural arrangements,[62,63] and potential soft phonon modes[64]—but the maps generated are also rich in information regarding chemical bonding. Here, we will show how the chemical pressure method can provide an alternative route to visualizing bonding that captures the forces leading to the cohesion between atoms, rather than proxies for bonding such as electron localization or electron density features. We will begin with a look at how covalent bonds are reflected in our chemical pressure maps of isolated molecules (H_2, CO_2, and S_8) and extended networks built from covalent bonds (graphene layer and C-diamond). Then we will move to van der Waals interactions in graphite, and hydrogen bonding in the ice-I_h phase of water. Finally, we will examine prototypical examples of metallic and ionic bonding, Na and NaH, respectively. Across these examples, distinct CP features will become associated with the various types of interatomic interactions in a way that combines the visual appeal of an ELF analysis with a strong affirmation of the physical significance of Ruedenberg's bonding picture.

TECHNICAL PROCEDURES

To make clearer the connection between CP maps and chemical bonding, it is useful to review the procedure by which these maps are constructed. For a periodic DFT calculation using pseudopotentials, the total energy can be expressed in the form:

$$E_{DFT} = \iiint_{cell} \left(\frac{1}{2} \sum_j f_j \left| \nabla \varphi_j(r) \right|^2 + V_{psp}\rho(r) + \frac{1}{2} V_{Hartree}\rho(r) + \epsilon_{XC}\rho(r) \right) d\tau$$

$$+ E_{nonlocal} + E_{Ewald} + E_a \qquad (1)$$

where f_j is the occupancy of the one-electron eigenfunction φ_j, $\rho(\mathbf{r})$ is the electron density, V_{psp} and $V_{Hartree}$ are the nondivergent components of the potential due to the local pseudopotential terms and the Hartree potential, $\epsilon_{XC}\rho(\mathbf{r})$ gives the contribution to the exchange-correlation from point $\mathbf{r}$. For the final terms, $E_{nonlocal}$ contains the potential energy contribution arising from the non-local components of the pseudopotential, and $E_{Ewald}+E_a$ together represent the electrostatic energy of the ionic pseudopotentials immersed in a homogeneous electron gas (incorporating terms from the electron-electron, electron-cation, and cation-cation interactions that would be divergent if calculated separately).

Many of the several components of the total energy may be represented as the integral over an energy density function, ρ_{energy}. These mappable terms allow us to define kinetic, Hartree, local pseudopotential and exchange-correlation energy densities:

$$\rho_{kinetic}(r) = \frac{1}{2} \sum_j f_j \left| \nabla \varphi_j \right|^2 \qquad (2)$$

$$\rho_{psp}(r) = V_{psp}\rho(r) \qquad (3)$$

$$\rho_{Hartree}(r) = V_{Hartree}\rho(r) \qquad (4)$$

$$\rho_{XC}(r) = \epsilon_{XC}\rho(r) \qquad (5)$$

which can be constructed from the output provided by a DFT calculation,[65] and combined to create an energy density function:

$$\rho_{energy} = \rho_{kinetic} + \rho_{psp} + \rho_{Hartree} + \rho_{xc} \qquad (6)$$

The remaining terms of the total energy do not easily breakdown into simple integrals over spatially varying functions.[66] In the chemical pressure approach, these are treated simply as a homogeneous background energy to create an energy map whose integral over the unit cell gives the correct total energy:

$$E_{DFT} = \iiint_{cell} \rho_{energy}\, d\tau + E_{remainder} \qquad (7)$$

When using the output of the DFT calculations, it is more convenient to approximate the integral in this equation as a sum over the grid used by the program for printing the electron density and potentials:

$$E_{DFT} \approx \sum_{n=1}^{N_v} \rho_{energy,n} V_v + E_{remainder} = \sum_{n=1}^{N_v} E_n + E_{remainder} \qquad (8)$$

where the n index runs over the N_v voxels (the volume elements associated with the grid points, i.e. the 3-D analogs of pixels) of volume V_v in which the unit cell volume is partitioned ($V_{cell} = N_v V_v$), E_n is the mapped energy associated with voxel n, and $E_{remainder}$ contains the total non-mapped contributions, whose role in CP analysis is described in detail in the Supporting Information to reference [67].

The key of the CP method is to note that this spatial resolution of the total energy allows a similar decomposition of the internal pressure:

$$P = -\frac{\partial E_{DFT}}{\partial V_{cell}} = -\frac{1}{N_v}\sum_{n=1}^{N_v} \frac{\partial E_n}{\partial V_v} - \frac{\partial E_{remainder}}{\partial V_{cell}}$$

$$= \frac{1}{N_v}\sum_{n=1}^{N_v} P_n + P_{remainder} \qquad (9)$$

where the macroscopic internal pressure is represented by an average over a pressure grid, with a homogeneous background pressure, $P_{remainder}$ (arising from the $E_{remainder}$ term of the energy), being added uniformly to all points of the pressure grid. Through this process, we obtain a map representing how different points in space respond energetically to a perturbation in the

2

volume of the system, which will offer a window into the forces underlying chemical bonds and other interatomic interactions.

The central step in this process is the calculation of partial derivatives of the voxel energies with respect to a grid's voxel volume, yielding the chemical pressure for each specific voxel (P_n). In practice, these voxel pressures can be obtained in the simplest way by taking the difference in energy for that voxel in structures that are slightly expanded (+) and contracted (-), isotropically:

$$P_n \cong -\frac{E_n^+ - E_n^-}{V_n^+ - V_n^-} \qquad (3)$$

Each of the energy density terms gives a corresponding contribution to the voxel pressures, meaning that individual maps can be made for, say, the kinetic energy and local pseudopotential components to the chemical pressure. The average over these grid pressures yields the system pressure, which for a material at equilibrium with its surroundings[68] will equal the external pressure. At zero pressure, this means that regions with negative and positive chemical pressure in a system should cancel each other to fulfil the mechanical equilibrium condition.

To apply this scheme to the various systems presented in this work, first-principles electronic structure calculations were performed under the formalism of DFT as implemented in the ABINIT program.[69,70] We used the LDA exchange-correlation functional of Goedecker, Teter, and Hutter,[71] and Hartswigen-Goedecker-Hutter (HGH) pseudopotentials.[72] Optimization of the corresponding unit cell geometries and atomic positions were performed with the Broyden-Fletcher-Goldfarb-Shanno minimization technique.[73] The structural relaxation was carried out until the maximal forces on the atoms were less than 5×10^{-5} Hartree/Bohr. Importantly, the same procedure was applied to all systems, meaning that no adjustments to the exchange-correlation functional were necessary for analyzing the various interaction types using the CP approach. Further details regarding to DFT calculations, including the cut-off energies and Monkhort-Pack k-point grids,[74] are provided in the Supporting Information.

Chemical Pressure maps were obtained by combining the output of three single-point calculations spanning a small volume range (usually ~3%) around the corresponding equilibrium crystal structure using the Fredrickson group CP package.[75] In all the cases, the core unwarping method was used to reduce the strong features around the cores (where the radial electron densities of free atoms are used as a guide to judging how much the voxel positions of the expanded and contracted structures are shifted relative to the atomic centers in equilibrium structure; this is the sole point where reference states enter the method).[75] The resulting CP maps were visualized with the VESTA program,[76] with pressure ranges on the color-maps tailored to reveal the features in the interactomic regions (with the large positive pressures in the core regions sometimes making ranges asymmetric around zero more convenient). Pressure values are given throughout the manuscript in atomic units unless specified otherwise.

RESULTS AND DISCUSSION

The DFT chemical pressure map for a material represents a spatial decomposition of the internal pressure. As this internal pressure contains all contributions establishing the equilibrium geometry of the structure, the bonding forces leading to the cohesion of solids and molecules should in some way be visible in these maps. A general answer as to how these forces should manifest in the CP maps is provided by noting that the net internal pressure is an average of regions with positive and negative CP. In regions of negative CP, a reduction of the system's volume would lower the local energy (as can be confirmed from Equation 3). This scenario suggests that the ion cores are packed too sparsely around the electrons. Areas of positive CP, by contrast, would be stabilized locally by the expansion of the system. Electrons are not so comfortable in these regions, as the atomic cores seem to be packed around them too

densely. In other words, the negative pressures regions, where the electron density *wishes* for a reduction of volume, are responsible for the attraction between the nuclei, while the positive pressure zones act to drive the nuclei apart. Thus, overall, we can expect negative CPs to be associated with bonds and attractive interactions, whereas positive CPs would be related to core electrons and repulsive interactions.

3.1. The simplest molecule: H_2. To begin seeing how forces of attraction and repulsion are manifested in CP maps, let's consider H_2, the simplest neutral molecule. This system is particularly interesting as it has no core electrons, and the electronic factors determining the interatomic distance will emerge entirely from the valence electrons. A look at the 2D slice through the CP map in Figure 1a reveals that these forces are not uniformly distributed: a continuous closed region of negative pressure contains the two H nuclei, with the values being especially low (blue) close to the two nuclei along the bonding path. The positive pressures, however, are located further outwards from the nuclei, beyond the black contour corresponding to CP=0. Overall, then, the forces leading to the cohesion between the H atoms are concentrated between the nuclei (reminiscent of the cartoon of electrons acting as glue holding the atoms together), with the drawbacks of bond formation being felt further out from the bonding region.

Several connections can be perceived between this CP map and the physics of chemical bond formation described by Ruedenberg.[49,77,78] In terms of the attractive region, note that the strongest attraction is not directly at the midpoint of the interatomic contact, but is instead concentrated near the two nuclei on opposite sides of the midpoint. This is a manifestation of the relationship between kinetic energy $\langle T \rangle$ and potential energy $\langle V \rangle$ encoded in the virial theorem: $\langle T \rangle = -\frac{1}{2}\langle V \rangle$ for system at its equilibrium geometry. The spreading of the wavefunction across the two nuclei lowers the kinetic energy cost of tightening the wavefunction around the nuclei (leading, in fact, to a negative kinetic energy contribution to the pressure in the internuclear region, Figure 1b). A deeper potential energy is thus attained for those electrons close to either of the nuclei in the space between atoms (Figure 1c). Following Ruedenberg, the positive kinetic chemical pressure located away from the bonding region close to the nuclear positions (Figure 1b) can also be understood: away from the internuclear region, the potential is more like that of the free atoms. The deviations from the free-atom wavefunctions induced by the bonding region are then, locally, perceived as a destabilizing perturbation.

While these two opposing effects cancel each other out at the equilibrium geometry, they are distributed in very different ways. The net attractive CP region is small but contains relatively large magnitudes, with the range of negative CP values being between -0.852 and 0.00 a.u. (1 a.u. = 29421 GPa, though in quoting numerical values we intend to illustrate trends rather than focus on magnitudes). The repulsive region, on the other hand, consists essentially of the rest of space, with very small values being spread over this expansive volume, between 0.00 and 0.007 a.u..

Another way of visualizing these features, which will become useful for the more complicated structures below, is through isosurfaces. In Figure 2a, CP isosurfaces for H_2 are shown of one positive and one negative selected CP value, +0.006 a.u. (white) and -0.01 a.u. (black), respectively, with the small magnitudes being chosen

so that the boundaries between the attractive and repulsive CP regions are charted. In this image, the cylindrical symmetry of the molecule is apparent, with the negative CP isosurface enclosing a volume containing the two nuclei as expected from the 2D plot. The positive isosurface, on the other hand, highlights the concentration of positive CP at the two ends of the molecule (resembling the antibonding molecular orbital) and in a ring running around the molecular equator.
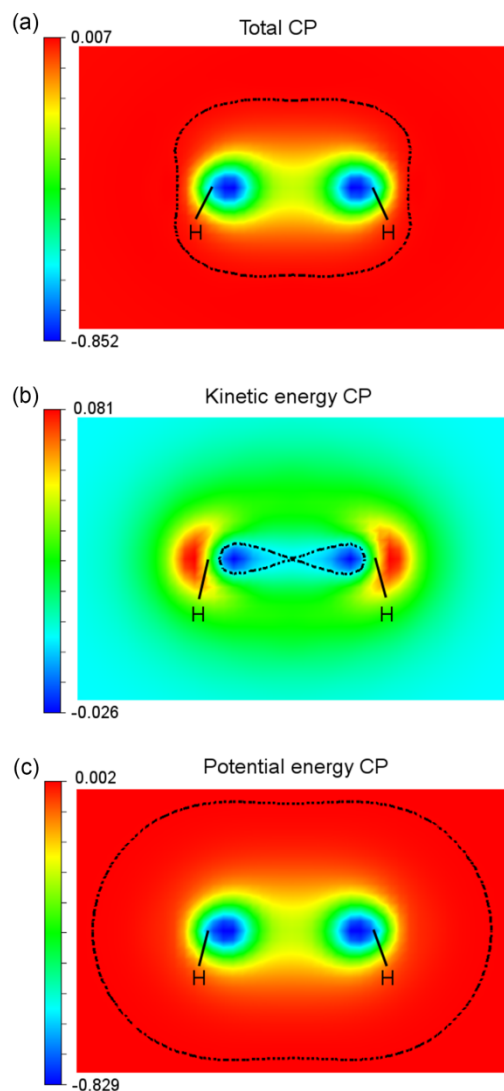
Figure 1. Chemical pressure (CP) analysis of the bonding within a H_2 molecule. (a) 2D cross-section of the total CP map through a plane containing the two H nuclei. (b) The corresponding cross-section of the kinetic energy contribution. (c) The potential energy contribution (total CP – explicit kinetic term). The CP = 0 contour is shown in black in all three panels. Pressures are given in atomic units.

The way in which these positive and negative CP features control the H-H bond distance can be visualized by following the evolution of the CP isosurfaces over a range of H-H distances at isosurfaces of ±0.008 a.u.. This process is carried out in Figure 2b for distances between 0.65 and 0.85 Å. At 0.85 Å, plot is dominated by the negative CP features. The overall negative CP experienced by the molecule (average = -0.74 a.u.) reflects that the distance is longer than the ideal. As the distance is decreased, the negative CP surface remains largely unchanged. By 0.70 Å, however, past the

equilibrium distance of 0.77 Å, positive CP features become apparent away from the bonding region. Finally, at 0.65 Å, the positive CPs grow to the point that the negative CP region begins to shrink, qualitatively agreeing with the overall positive pressure now calculated for the molecule.
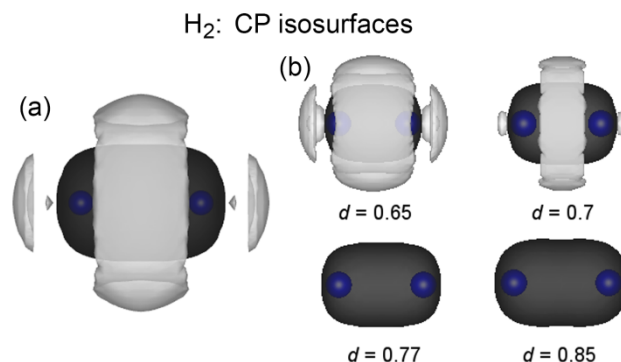

Figure 2. CP distributions within the H_2 molecule visualized with isosurfaces. (a) 3D isosurfaces with CP=+0.006 (white) and CP=-0.01 (black) for the H_2 molecule in its equilibrium geometry. (b) H-H distance dependence of the CP distribution. Isosurface values: CP=+0.008 (white) and CP=-0.008 (black). Pressures are given in atomic units, while the distances are listed in Å.

3.2. More complicated molecules: CO_2 and S_8. As we move beyond H_2, one major difference is going to be the introduction of multiple shells and subshells of electrons for heavier atoms (though, to some extent, the effects of the core electrons will be folded into the pseudopotential cores). Such features are illustrated by the CO_2 molecule (Figure 3). As can be seen most easily in the CP profile across the molecule (Figure 3b), deep wells of negative CP occur along the C-O contacts serving as the attractive component of the C-O interactions. As for H_2, the minima along the bond do not lie at the center of the bonding region, but instead occur closer to the nuclei on the two sides of the bond. This time, however, the minima closer to the O atoms are significantly deeper, consistent with the O atom's higher electronegativity and the polarity of the C-O bonds.

Several other new features are also apparent here. While in H_2 the positive CPs were spread out through the external area of the molecule, now they are concentrated into peaks centered on the C and O nuclei. The core regions now contain the major restoring force acting against the bonding regions' call for the contraction of the molecule. In addition, smaller positive CPs also occur at the outskirts of the molecules (as is always seen for isolated molecules).

Another new entity appearing in CO_2 is a well of negative CP projecting from the O atoms outwards along the axis of the molecule. In shape and orientation, these negative CP lobes resemble the sp-hybridized lone-pairs that are commonly drawn for the CO_2 molecule (Figure 3a). Given the common association of lone-pairs with repulsion, as in the valence shell electron-pair repulsion (VSEPR) model,[79] assignment of negative CP to a lone-pair may be at first surprising. One explanation for how the lone-pair region can drive the contraction of the molecule is in how the electrons of the C-O bonds are distributed. They are focused in the C-O bonding region, opening access to the core on the opposite side of the O atoms. The enhancement of this effect upon the contraction of the molecule would then lead to the stabilization of the electrons in the

O lone-pair region, which would be reflected as negative pressure in the CP map. This view gives an alternative interpretation of the usefulness of the VSEPR model: electron pairs tend to maximize their distance from each other to support access to the cationic core from different angles, rather than due to direct Coulombic repulsion between them.
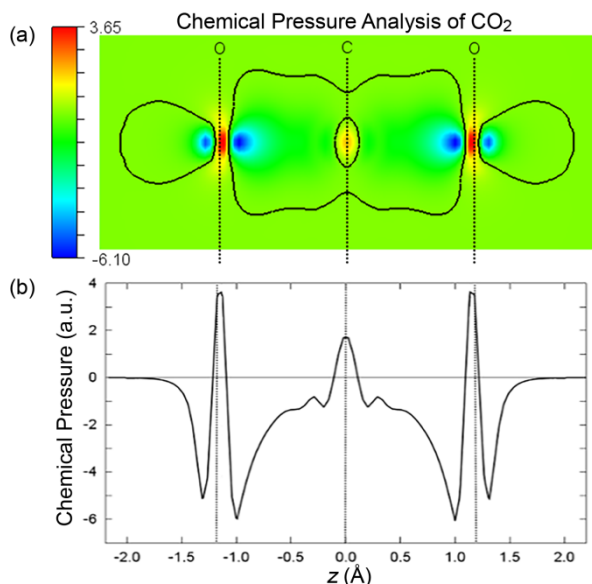
Figure 3. Chemical pressure (CP) analysis of a CO_2 molecule. (a) 2D cross-section of the CP map calculated for the molecule. A black contour is shown for CP=0. (b) 1D profile of CP map along the axis of the CO_2 molecule.

The generality of these features for covalent systems can be seen in our last molecular example, the S_8 crown molecule. Taking a horizontal cross section through the molecule's boat-like geometry yields the 2D CP map of Figure 4a. Each S-S contact appears with a blue dumbbell of negative CP similar to that observed for H_2, but with the minima now closer to the bond centers. In the 3D plot, these negative pressure features now manifest as black peanut-like shapes representing the S-S bonds, as well as a black lobe pointing outwards from each S atoms coinciding in space with the expected positions of sp^2-hybridized lone-pairs. The strongest positive pressures (red in the 2D plot, white surfaces in the 3D plot of Figure 4b) are associated with electron densities around the nuclear positions. As with H_2 and CO_2, the CP distributions allow not only a visualization of the chemical bonds, but put them in the context of a balance of forces within the molecule.

3.3. Infinite 2D and 3D Lattices Built from Covalent Bonds. The themes we saw above continue uninterrupted when we build up from simple molecules to infinite lattices connected through covalent bonds. One simple example is graphene, in which a single honeycomb net of carbon atoms is held together through σ bonds and a delocalized π system. The 2D and 3D CP maps (Figure 5) again show negative CP along the bonded contacts, with the CP features necking at the bond centers. This creates a trefoil pattern of negative CP around each C atom mirroring its sp^2-hybridization.

The most of the positive CP is localized around C nuclear positions, largely filling in whatever space is leftover by the C-C σ bonds. These positive CP features create a cloud of positive pressure above and below the carbon layer. Indeed for a CP value of

+0.01 a.u., a continuous non-planar surface tracing out the atomic positions is obtained.
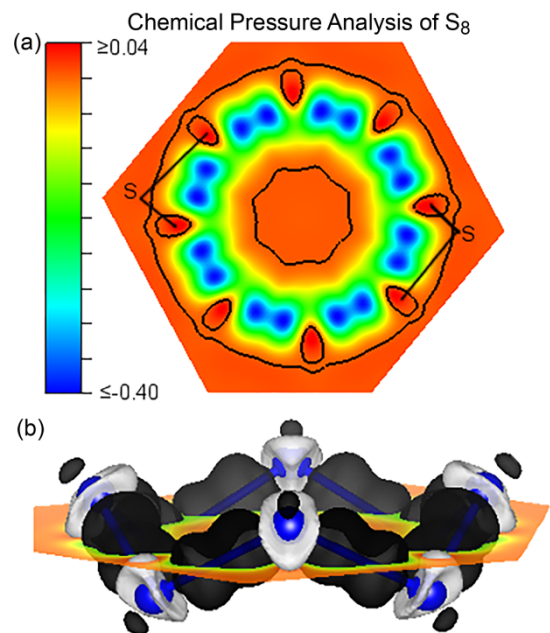
Figure 4. Chemical pressure plots of a S_8 molecule. (a) 2D cross-section along the plane intersecting the eight S-S bonds. Black curves: CP=0 contour. (b) 3D isosurfaces with CP=+0.02 (white) and CP=-0.17 (black).
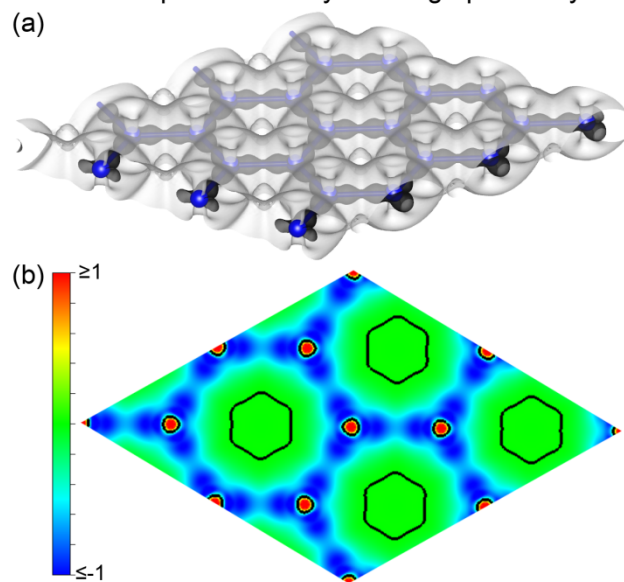
Figure 5. Chemical pressure (CP) analysis of graphene. (a) 3D isosurfaces with CP=+0.01 (white) and CP=-0.6 (black). (b) 2D map of the plane containing the C atoms. Black curves: CP=0 contour.

Curiously, no appreciable negative CP is detected here for the π interactions along the graphene layer. However, just above and below the C atoms, pits in the positive CP isosurface can be detected. These depressions may reflect the stabilization of the π electrons as π overlap allows them to grip more tightly to the C cores. The overlap of these regions with the positive CP components of the σ interactions would then prevent strong negative CP features from appearing at these points.

5
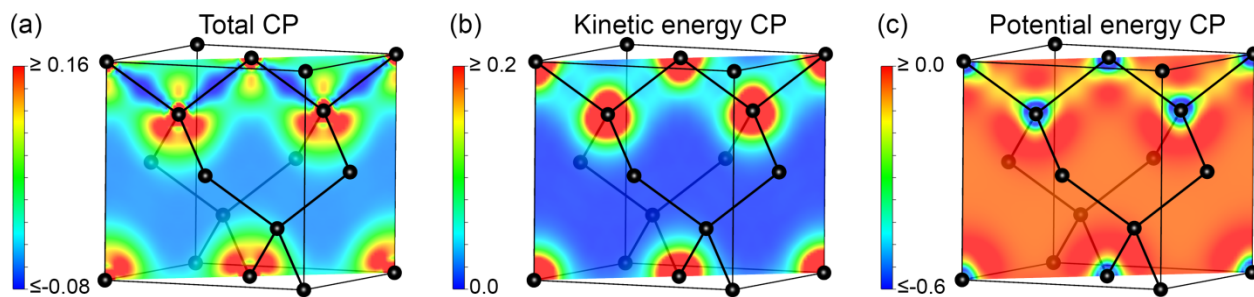
Figure 6. Chemical pressure maps of the diamond polymorph of C. (110) cross-sections are shown for (a) the total CP, (b) the kinetic energy component of the CP, and (c) the potential energy contribution to the CP.

The CP map of the diamond form of carbon, the quintessential covalent solid, can be understood in a similar fashion (Figure 6). Negative CP features are again focused in the bonding regions along the C-C contacts, with positive CP poking out from the cores into the spaces between the bonds. As is shown with a (110) cross-section, the negative CPs between the C atoms show peaks close to the cores as in graphene. These are somewhat dwarfed, however, by a new feature: a CP minimum directly at the bond center, which is less understandable from the Ruedenberg model.

The origin of this CP pattern can be discerned by separately plotting the kinetic energy and potential energy contributions (Figure 6). In the potential energy component (Figure 6c) deep CP wells along the C-C contacts again appear nearer the atomic cores, visible here as green protrusions for the cores. This potential energy stabilization near the atomic centers is in-line with our expectations from the previous analyses. The difference arises from the kinetic energy contribution, which is dominated by a relatively isotropic accumulation of positive CP in the core region. Unlike the molecules and materials we have looked at so far, where the small number of interatomic contacts to each atom allowed spaces for the positive pressures to collect away from the bonding interactions, the C cores are being squeezed from four different directions, with significant overlap between the positive and negative CP components near the cores being unavoidable. When these positive and negative components are summed, the bond centers (where the kinetic energy term is small) end up with the largest net negative CP.

3.4. Graphite: A system displaying both intra- and inter-molecular interactions. So far, we have focused on structures whose atoms are linked together through covalent bonds. For molecules or the graphene sheets we discussed, these would often engage in interactions with other molecules through non-covalent forces, such as van der Waals forces. An analysis of the graphite structure, built from an ABAB stacking of graphene layers held together with weak van der Waals interlayer interactions, offers an opportunity to explore how such intermolecular interactions are manifested in the CP function.

We begin with the optimization of the graphite structure using LDA and HGH norm-conserving pseudopotentials. This relaxation leads to a structure whose balance between intralayer and interlayer distances are quite similar to those obtained in experiment. In particular, the c/a ratio for the cell parameters optimizes to 2.718 while the experimental ratio is 2.724.[79] This level of agreement is somewhat surprising given the well-known limitations of using standard DFT to treat van der Waals interactions,[80,81] but it is not

unprecedented when applying this methodology to graphite.[82] As such, we then proceed to explore the LDA CP features of graphite calculated with the goal of seeing qualitatively how the interlayer cohesion is reflected in the maps.

The CP map of graphite is shown both as a cross-section through a single layer and with isosurfaces for 3D structure in Figure 7. Within the individual layers, the CP distribution is very similar to that of the isolated layer, emphasizing the secondary nature of the inter-layer interactions. Each C atom has three wells of negative CP, one directed toward each of its C neighbors in the sheet. The remaining space around the C core is taken up by positive CP, corresponding to regions of space where the deviations from the wavefunction away from the atomic orbitals of a free atom are not compensated by bond formation.
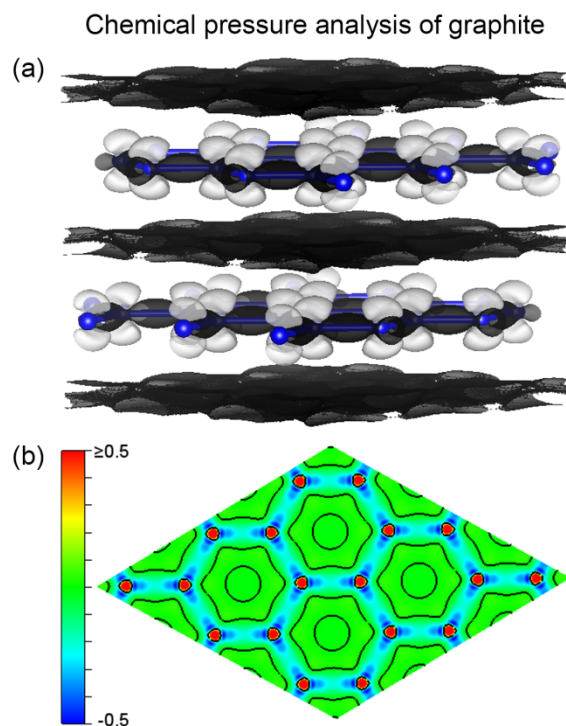

Figure 7. Chemical pressure plots of graphite. (a) 3D isosurfaces with CP=+0.07 (white) and CP=-0.02 (black). (b) 2D map of the (001) plane containing C atoms.

The major differences between the CP features of graphene and graphite appear instead at the surfaces of the layers. In graphene, the spaces above and below the graphene layer exhibit positive CPs, again arising from the perturbations to the C atoms to allow C-C

bond formation. In graphite, this situation changes, with negative CPs now occurring between the sheets. The presence of negative pressure in this interlayer region is reassuring, as it suggests an attractive force is holding the layers together.

3.5. Chemical pressures of the hydrogen bond. We now turn to another type of intermolecular interaction, the hydrogen bond. These interactions have often been considered as being primarily electrostatic in nature, with the partial positive charge of a H atom in an X-H bond (X = O, N, F, or other electronegative atom) being attracted to the lone-pair of a nearby atom. This picture, however, has been enriched by theoretical calculations and experimental data such as NMR coupling constants, which show that hydrogen bonds can have a quantum mechanical component,[83-86] most easily understood in terms of the partial donation of the lone-pair into the X-H σ^* orbital.[87] Features corresponding to hydrogen bonds are readily seen in the CP maps, as we will now demonstrate using the low pressure I_h phase of ice.

In this structure, the oxygen atoms exhibit the typical four-fold coordination by H atoms forming a distorted tetrahedron in which two hydrogen atoms are covalently bonded while the other two come from neighboring molecules. A 2D cross-section of the CP map through a plane contacting O-H and O···H interactions is shown in (Figure 8). The red color in the map is associated with the positive pressure regions surrounding the oxygen position, while the covalent O-H bonds are marked by an intense blue color indicating the negative CP we normally associate with bonds. More importantly, though, a narrow channel of negative pressure extends from the O-H bond along the O-H···O axis into the region associated with the hydrogen bond.
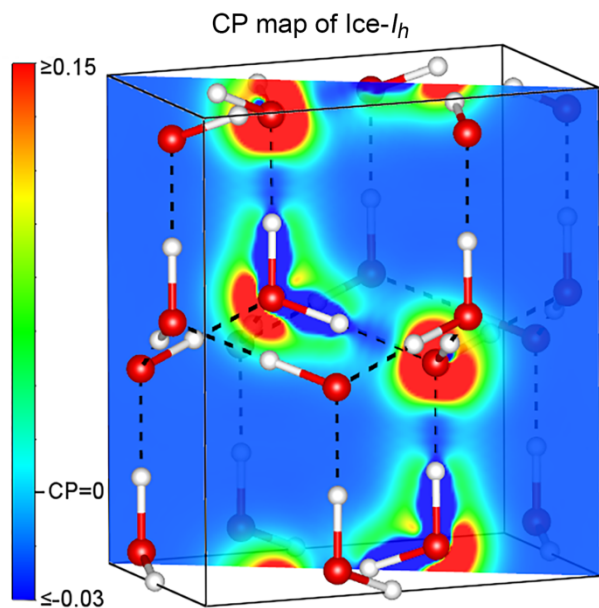
Figure 8. Chemical pressure analysis of Ice-I_h. A (1-10) cross-section of the CP map is shown containing O-H covalent bonds and H···O hydrogen bonds. Red and white spheres indicate oxygen and hydrogen atoms, respectively.

The relative scales of these interactions are more clearly illustrated in a 1D profile of the CP function along a O-H···O path (Figure 9). Here, the covalent bond appears as a deep double well of negative pressure, with the H atom situated toward the outside of one of these wells. The hydrogen bond region is much more shallow, and almost resembles an extension of the negative CP of the covalent bond into the intermolecular region. As regards the partition into contributions, we can observe, again, that the positive pressure around oxygen cores arises from the kinetic energy term. The negative pressure in the O–H bond, meanwhile, is due to the potential energy term, which is prolonged along the H-bond direction.
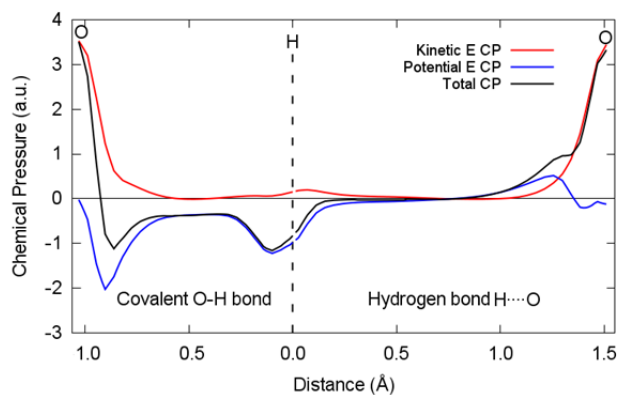
Figure 9. 1D profile of the chemical pressure contributions along the O-H···O bond path of water in the Ice-I_h phase.

One new feature that we see in the hydrogen-bond region is a shoulder of positive pressure stemming from the O atom arising from the potential energy, which contrasts sharply with the negative local contribution we have generally observed for covalent interactions. This potential energy repulsion is reminiscent of the situation described by Feinberg and Ruedenberg for long-range interactions in an H_2^+ ion stretched far past its equilibrium bond length, where the stabilization relative to dissociated species is restricted to the kinetic energy.[50] In our future work, we will explore the role of such positive CP shoulders in non-covalent interactions more generally.

**3.6. Signatures of Metallic and Ionic Bonding in CP Maps.** Now that we have considered a number of examples involving covalent bonds, let's briefly explore how the other two basic types of chemical bonding—metallic and ionic—are reflected in chemical pressure maps. To hone in on the essential CP features for each of these cases, we will consider very simple examples in which only valence electrons relevant to the bonding are explicitly included: Na metal and NaH. In both phases, each atom contributes only a single valence electron which either becomes part of a delocalized electron gas (metallic bonding) or sticks close to the most electronegative cores (ionic bonding).

In Figure 10, we begin with a look at the CP scheme of Na metal in the body-centered cubic (bcc) structure. The overall CP map (Figure 10a) aligns closely with the features that have been seen in the CP schemes for many other metallic phases:[75] the cores appear with concentric, nearly spherical shells of intense pressures that are positive overall. These core features are set against a much flatter, slightly negative background. The positive CPs on the cores and negative CP in the interstitial spaces average out to a pressure of zero over the whole unit cell at the equilibrium geometry.

Within the negative background, more subtle features are visible whose locations suggest chemical significance. In particular, within the (110) cross section shown, slight minima can be detected at the midpoints along the first-nearest neighbor contacts (across the

7
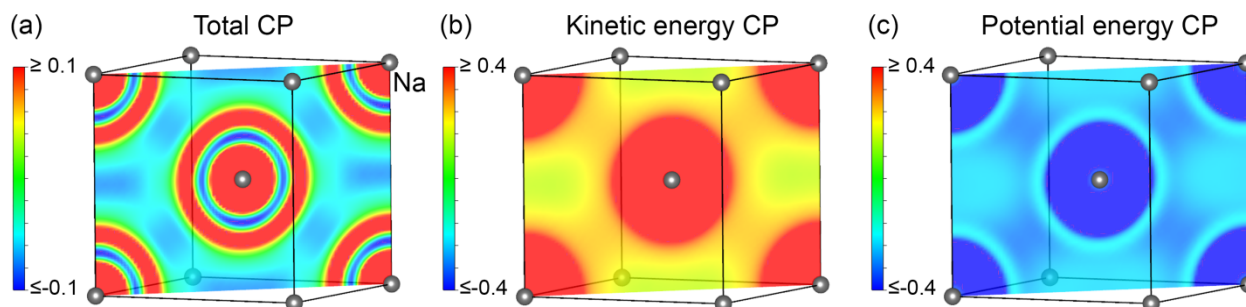
Figure 10. Cross-sections of the chemical pressure (CP) map for bcc-Na metal, showing (a) the total CP distribution alongside its (b) kinetic energy and (c) potential energy components. Pressures are given in thousandths of an a.u..
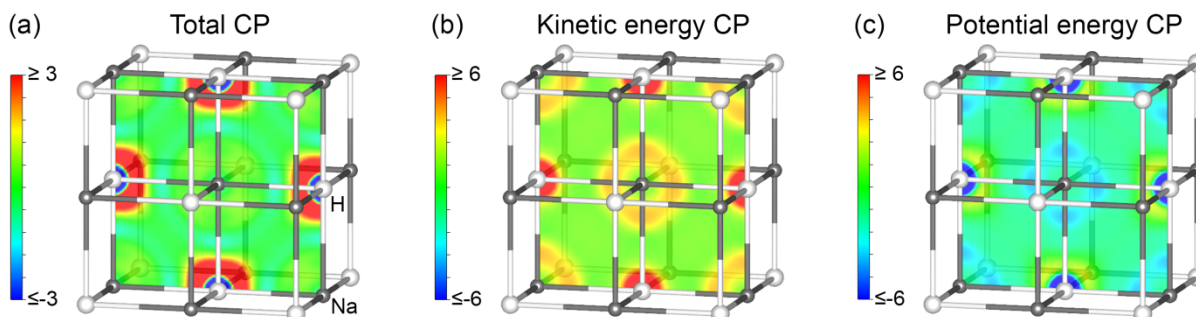
Figure 11. Chemical pressure plots of ionic NaH in the rocksalt structure. Cross sections are provided of (a) the total CP map, as well as its (b) kinetic and (c) potential energy components. Numerical values are in thousandths of an a.u.

body-diagonals) and second near-neighbor contacts (along the cell edges). While these two depressions in the map seem similar at first glance, a look at the potential and kinetic energy contributions to the map separately reveals that they have different origins (Figures 10b and 10c). The potential energy plot shows shallow pockets of negative CP with a faint hourglass pattern resembling the double minima we saw above for covalent bonds. These negative wells, however, are weak compared to the positive kinetic energy pressures emanating from the cores, so that the total CP shows only a weak minimum along the nearest-neighbor contacts.

Along the second nearest neighbor contacts, the same overall result is obtained in a different way: the potential energy CP is largely flat along the contact, providing little influence on the shape of the total CP distribution in this area. Instead the low CP at the midpoint between the atoms here results simply from a valley in the kinetic energy term due to relatively long distance to any of the atomic cores. Indeed, what appears as a minimum in the CP between second-nearest neighbors is in fact a continuous distribution that passes through the interstitial regions of the structure: in these areas the flat negative Ewald pressure predominates over the core pressures. This picture aligns with the classic picture for a metal of ion cores held together by their attraction to the electron gas that surrounds them.

From the point of view of CP analysis, the difference between metallic and covalent bonding can thus be seen in the nature of the driving forces competing for the expansion and contraction of the structure. For the covalent bond, this competition was essentially between the enhanced stability of electrons concentrating near the cores along the interatomic vectors against the kinetic energy costs that the wavefunctions feel away from the bonding region. In the metal, however, the primary balance occurs instead between the

kinetic energy costs of squeezing the cores against the electrostatic attraction between the cores and the electron gas (which belongs to the Ewald term of the total energy).

The CP scheme for our model ionic system, NaH, shows similarly non-directional features (Figure 11). As in Na metal, positive CP is localized around atomic centers, while the interstitial spaces provide a flatter negative pressure background. Unlike Na metal, however, the positive pressures are not distributed evenly over the atoms: the H atoms (white) exhibit intense CPs while much less activity is evident on the Na cores. This difference is, of course, consistent with the ionicity of the compound, in which all valence electrons are envisioned as belonging to the H$^-$ anions, leaving behind bare Na$^+$ ions.

A look at the separate potential and kinetic energy contributions to the CP provides further details in to the forces competing within the structure (Figures 11b and 11c). The kinetic energy contributions are peaked at the H positions, and to a smaller degree around the Na cores—typical features for the core regions of atoms—with little indication of the wells along specific interatomic contacts expected for a localized interaction. The potential energy pressure, meanwhile, exhibits negative CPs around the Na positions and positive CPs around the H (except for very negative CPs very close the nucleus), all against a flat negative background.

Altogether, these features tell of a packing of spherical ions held together by electrostatic attraction (depicted here as the flat background pressure arising from the Ewald term) and some back donation from the H$^-$ anions to Na$^+$ cations (negative potential energy CP on Na$^+$ centers), which is resisted by positive pressures on the H$^-$ anions. If we interpret the positive CPs on the H$^-$ anions in terms of anion-anion repulsion, we arrive at the common notion of

ionic crystals as based on close-packings of anions stabilized by attraction to cations in the interstitial positions.[88]

4. CONCLUSIONS

In this Article, we have explored how the DFT Chemical Pressure (CP) method can form the basis of the visualization of the forces within chemical bonds. Over a series of molecular and crystalline examples, specific features in the CP maps have become associated with different types of bonding interactions. Focused concentrations of negative pressures along an interatomic contact (countered by positive pressures near the cores) correlated strongly with the presence of covalent bonds, while weaker intermolecular interactions, such as van der Waals attraction and hydrogen bonds, were reflected in much shallower negative CP features. Model systems for metallic and ionic bonding, meanwhile, exhibited much less directional interactions, with the major balance of forces being between positive CPs around the ion cores and a background negative pressure representing the long-range electrostatic forces. Through these examples, we demonstrated the ability of the CP approach to simultaneously visualize a range of interaction types, e.g. covalent bonds and weaker non-covalent interactions present in the same system.

In each of these systems, but most particularly the covalent cases, the CP features provided images quite similar to those that would be obtained with another method for visualizing bonding features: the electron localization function. With the CP approach, however, these features now have visual and accessible interpretations in terms of forces calling for the expansion and contraction of the structures, which can be investigated in more detail by separately plotting different energetic contributions to the CP map, such as the kinetic and potential energy terms. The pictures that result for the covalent bond closely align with the model for the chemical bond described in detail by Ruedenberg and coworkers for simple molecular systems such as H_2^+, and offer the opportunities for similar levels of insight to be attained for more complex systems. We are looking forward to seeing what the CP-based bond analysis may reveal for a broader range of bonding situations, such as strained molecules, the skeletal bonding in cluster compounds, and the isolobal bonds of intermetallic phases.

ASSOCIATED CONTENT

Supporting Information. Additional computational details, including energy cut-offs, k-point grids, tables of optimized atomic coordinates and total energies; comparison of 1D profiles of the CP maps of graphite and graphene; isosurface of the CP map of ice-I_h.

AUTHOR INFORMATION

Corresponding Author

* E-mail: danny@chem.wisc.edu, jmrecio@uniovi.es

ACKNOWLEDGMENT

REFERENCES

(1) Needham, P. The Source of Chemical Bonding, *Stud. Hist. Philos. Sci. A* **2014**, *45*, 1-13.

(2) Foster, J. M.; Boys, S. F. Canonical Configurational Interaction Procedure, *Rev. Mod. Phys.* **1960**, *32*, 300-302.

(3) Yannello, V. J.; Kilduff, B. J.; Fredrickson, D. C. Isolobal Analogies in Intermetallics: The Reversed Approximation MO Approach and Applications to CrGa$_4$- and Ir$_3$Ge$_7$-Type Phases, *Inorg. Chem.* **2014**, *53*, 2730-2741.

(4) Yee, K. A.; Hughbanks, T. Utility of Semilocalized Bonding Schemes in Extended Systems: Three-center Metal-metal Bonding in Molybdenum Sulfide (MoS$_2$), Niobium Tantalum Sulfide Bronze (H$_x$(Nb,Ta)S$_2$), and Zirconium Sulfide (ZrS), *Inorg. Chem.* **1991**, *30*, 2321-2328.

(5) Wannier, G. H. The Structure of Electronic Excitation Levels in Insulating Crystals, *Phys. Rev.* **1937**, *52*, 191-197.

(6) Zurek, E.; Jepsen, O.; Andersen, O. K. Muffin-tin Orbital Wannier-like Functions for Insulators and Metals, *ChemPhysChem* **2005**, *6*, 1934-1942.

(7) Zurek, E.; Jepsen, O.; Andersen, O. K. Searching for the Interlayer Band and Unravelling the Bonding in β-ThSi$_2$ and α-ThSi$_2$ with NMTO Wannier-like Functions, *Inorg. Chem.* **2010**, *49*, 1384-1396.

(8) Marzari, N.; Mostofi, A. A.; Yates, J. R.; Souza, I.; Vanderbilt, D. Maximally Localized Wannier functions: Theory and Applications, *Rev. Mod. Phys.* **2012**, *84*, 1419-1475.

(9) Hughbanks, T.; Hoffmann, R. Chains of Trans-edge-sharing Molybdenum Octahedra: Metal-metal Bonding in Extended Systems, *J. Am. Chem. Soc.* **1983**, *105*, 3528-3537.

(10) Hughbanks, T.; Hoffmann, R. Molybdenum Chalcogenides: Clusters, Chains, and Extended Solids. The Approach to Bonding in Three Dimensions, *J. Am. Chem. Soc.* **1983**, *105*, 1150-1162.

(11) West, A. C.; Schmidt, M. W.; Gordon, M. S.; Ruedenberg, K. A comprehensive analysis of molecule-intrinsic quasi-atomic, bonding, and correlating orbitals. I. Hartree-Fock wave functions, *J. Chem. Phys.* **2013**, *139*, 234107.

(12) West, A. C.; Schmidt, M. W.; Gordon, M. S.; Ruedenberg, K. A Comprehensive Analysis in Terms of Molecule-Intrinsic, Quasi-Atomic Orbitals. II. Strongly Correlated MCSCF Wave Functions, *J. Phys. Chem. A* **2015**, *119*, 10360-10367.

(13) Foster, J. P.; Weinhold, F. Natural Hybrid Orbitals, *J. Am. Chem. Soc.* **1980**, *102*, 7211-7218.

(14) Reed, A. E.; Weinhold, F. Natural Localized Molecular Orbitals, *J. Chem. Phys.* **1985**, *83*, 1736-1740.

(15) Reed, A. E.; Curtiss, L. A.; Weinhold, F. Intermolecular Interactions from a Natural Bond Orbital, Donor-acceptor Viewpoint, *Chem. Rev.* **1988**, *88*, 899-926.

(16) Weinhold, F.; Landis, C. R. *Valency and Bonding: A Natural Bond Orbital Donor-acceptor Perspective*; Cambridge University Press: Cambridge, UK ; New York, 2005.

(17) Weinhold, F.; Landis, C. R. *Discovering Chemistry with Natural Bond Orbitals*; Wiley: Hoboken, NJ, 2012.

(18) Galeev, T. R.; Dunnington, B. D.; Schmidt, J. R.; Boldyrev, A. I. Solid State Adaptive Natural Density Partitioning: A Tool for Deciphering Multi-center Bonding in Periodic Systems, *PCCP* **2013**, *15*, 5022-5029.

(19) Dolyniuk, J.-A.; He, H.; Ivanov, A. S.; Boldyrev, A. I.; Bobev, S.; Kovnir, K. Ba and Sr Binary Phosphides: Synthesis, Crystal Structures, and Bonding Analysis, *Inorg. Chem.* **2015**, *54*, 8608-8616.

(20) Bader, R. F. W. *Atoms in Molecules: A Quantum Theory*; Oxford University Press: Oxford, England, 1990.

(21) Johnson, E. R.; Keinan, S.; Mori-Sánchez, P.; Contreras-García, J.; Cohen, A. J.; Yang, W. Revealing Noncovalent Interactions, *J. Am. Chem. Soc.* **2010**, *132*, 6498-6506.

(22) Becke, A. D.; Edgecombe, K. E. A Simple Measure of Electron Localization in Atomic and Molecular Systems, *J. Chem. Phys.* **1990**, *92*, 5397-5403.

9

(23) Savin, A.; Becke, A. D.; Flad, J.; Nesper, R.; Preuss, H.; Von Schnering, H. G. A New Look at Electron Localization, *Angew. Chem. Int. Ed.* **1991**, *39*, 409-412.

(24) Savin, A.; Nesper, R.; Wengert, S.; Fassler, T. F. ELF: The Electron Localization Function, *Angew. Chem. Int. Ed.* **1997**, *36*, 1808-1832.

(25) Kohout, M.; Pernal, K.; Wagner, F. R.; Grin, Y. Electron Localizability Indicator for Correlated Wavefunctions. I. Parallel-spin Pairs, *Theor. Chem. Acc.* **2004**, *112*, 453-459.

(26) Savin, A. The Electron Localization Function (ELF) and its Relatives: Interpretations and Difficulties, *J. Mol. Struct.: THEOCHEM* **2005**, *727*, 127-131.

(27) Silvi, B.; Savin, A. Classification of Chemical Bonds Based on Topological Analysis of Electron Localization Functions, *Nature* **1994**, *371*, 683-686.

(28) Wagner, F. R.; Bezugly, V.; Kohout, M.; Grin, Y. Charge Decomposition Analysis of the Electron Localizability Indicator: A bridge between the Orbital and Direct Space Representation of the Chemical Bond, *Chem. Eur. J.* **2007**, *13*, 5724-5741.

(29) Hopffgarten, M. v.; Frenking, G. Energy Decomposition Analysis, *Wiley Interdiscip. Rev. Comput. Mol. Sci.* **2012**, *2*, 43-62.

(30) Wang, F.; Miller, G. J. Revisiting the Zintl-Klemm Concept: Alkali Metal Trielides, *Inorg. Chem.* **2011**, *50*, 7625-7636.

(31) Dronskowski, R.; Bloechl, P. E. Crystal Orbital Hamilton Populations (COHP): Energy-resolved Visualization of Chemical Bonding in Solids Based on Density-functional Calculations, *J. Phys. Chem.* **1993**, *97*, 8617-8624.

(32) Burdett, J. K. *Molecular shapes : theoretical models of inorganic stereochemistry*; Wiley: New York, 1980.

(33) Hoffmann, R. *Solids and Surfaces: A Chemist's View of Bonding in Extended Structures*; VCH Publishers: New York, NY, 1988.

(34) Burdett, J. K. *Chemical Bonding in Solids*; Oxford University Press: New York, 1995.

(35) Gonthier, J. F.; Steinmann, S. N.; Wodrich, M. D.; Corminboeuf, C. Quantification of "fuzzy" chemical concepts: a computational perspective, *Chem. Soc. Rev.* **2012**, *41*, 4671-4687.

(36) *Applications of Topological Methods in Molecular Chemistry*; Chauvin;, R.; Lepetit;, C.; Silvi;, B.; Alikhani, E., Eds.; Springer International Publishing: Switzerland, 2016.

(37) Mayer, I. *Bond orders and energy components: extracting chemical information from molecular wave functions*; CRC Press: Boca Raton, 2016.

(38) Bader, R. F. W.; Hernández-Trujillo, J.; Cortés-Guzmán, F. Chemical bonding: From Lewis to atoms in molecules, *J. Comput. Chem.* **2007**, *28*, 4-14.

(39) Schmidt, M. W.; Ivanic, J.; Ruedenberg, K. Covalent Bonds are Created by the Drive of Electron Waves to Lower their Kinetic Energy through Expansion, *J. Chem. Phys.* **2014**, *140*, 204104.

(40) Schmidt, M. W.; Ivanic, J.; Ruedenberg, K. The Physical Origin of Covalent Bonding, In *The Chemical Bond*; Wiley-VCH Verlag GmbH & Co. KGaA: 2014, p 1-68.

(41) Bader, R. F. W. On the non-existence of parallel universes in chemistry, *Foundations of Chemistry* **2011**, *13*, 11-37.

(42) Fredrickson, D. C. Electronic Packing Frustration in Complex Intermetallic Structures: The Role of Chemical Pressure in Ca$_2$Ag$_7$, *J. Am. Chem. Soc.* **2011**, *133*, 10070-10073.

(43) de Silva, P.; Corminboeuf, C. Simultaneous Visualization of Covalent and Noncovalent Interactions Using Regions of Density Overlap, *J. Chem. Theory Comput.* **2014**, *10*, 3745-3756.

(44) Popelier, P. L. A. Quantum Chemical Topology, In *The Chemical Bond II: 100 Years Old and Getting Stronger*; Mingos, D. M. P., Ed.; Springer International Publishing: Cham, 2016, p 71-117.

(45) Schmider, H. L.; Becke, A. D. Chemical content of the kinetic energy density, *Journal of Molecular Structure: THEOCHEM* **2000**, *527*, 51-61.

(46) Jeziorski, B.; Moszynski, R.; Szalewicz, K. Perturbation theory approach to intermolecular potential energy surfaces of van der Waals complexes, *Chem. Rev.* **1994**, *94*, 1887-1930.

(47) Morokuma, K. Molecular Orbital Studies of Hydrogen Bonds. III. C=O···H–O Hydrogen Bond in H2CO···H2O and H2CO···2H2O, *The Journal of Chemical Physics* **1971**, *55*, 1236-1244.

(48) Pendás, A. M.; Blanco, M. A.; Francisco, E. Chemical fragments in real space: Definitions, properties, and energetic decompositions, *J. Comput. Chem.* **2007**, *28*, 161-184.

(49) Ruedenberg, K. The Physical Nature of the Chemical Bond, *Rev. Mod. Phys.* **1962**, *34*, 326-376.

(50) Feinberg, M. J.; Ruedenberg, K. Paradoxical Role of the Kinetic-Energy Operator in the Formation of the Covalent Bond, *J. Chem. Phys.* **1971**, *54*, 1495-1511.

(51) Feinberg, M. J.; Ruedenberg, K.; Mehler, E. L. The Origin of Binding and Antibinding in the Hydrogen Molecule-Ion, In *Adv. Quantum Chem.*; Per-Olov, L., Ed.; Academic Press: 1970; Vol. Volume 5, p 27-98.

(52) Bacskay, G. B.; Nordholm, S. Covalent Bonding: The Fundamental Role of the Kinetic Energy, *J. Phys. Chem. A* **2013**, *117*, 7946-7958.

(53) Kutzelnigg, W.; Schwarz, W. H. E. Formation of the chemical bond and orbital contraction, *Phys. Rev. A* **1982**, *26*, 2361-2367.

(54) Goddard, W. A.; Wilson, C. W. The Role of Kinetic Energy in Chemical Binding, *Theoret. Chim. Acta* **1972**, *26*, 211-230.

(55) West, A. C.; Schmidt, M. W.; Gordon, M. S.; Ruedenberg, K. Intrinsic Resolution of Molecular Electronic Wave Functions and Energies in Terms of Quasi-atoms and Their Interactions, *J. Phys. Chem. A* **2017**, *121*, 1086-1105.

(56) Nielsen, O. H.; Martin, R. M. Quantum-mechanical Theory of Stress and Force, *Phys. Rev. B* **1985**, *32*, 3780-3791.

(57) Godfrey, M. J. Stress Field in Quantum Systems, *Phys. Rev. B* **1988**, *37*, 10176-10183.

(58) Ziesche, P.; Gräfenstein, J.; Nielsen, O. H. Quantum-mechanical Stress and a Generalized Virial Theorem for Clusters and Solids, *Phys. Rev. B* **1988**, *37*, 8167-8178.

(59) Filippetti, A.; Fiorentini, V. Theory and Applications of the Stress Density, *Phys. Rev. B* **2000**, *61*, 8433-8442.

(60) Rogers, C. L.; Rappe, A. M. Geometric Formulation of Quantum Stress Fields, *Phys. Rev. B* **2002**, *65*, 224117.

(61) Kilduff, B. J.; Fredrickson, D. C. Chemical Pressure-Driven Incommensurability in CaPd$_5$: Clues to High-Pressure Chemistry Offered by Complex Intermetallics, *Inorg. Chem.* **2016**, *55*, 6781-6793.

(62) Berns, V. M.; Fredrickson, D. C. Problem Solving with Pentagons: Tsai-Type Quasicrystal as a Structural Response to Chemical Pressure, *Inorg. Chem.* **2013**, *52*, 12875-12877.

(63) Berns, V. M.; Fredrickson, D. C. Structural Plasticity: How Intermetallics Deform Themselves in Response to Chemical Pressure, and the Complex Structures That Result, *Inorg. Chem.* **2014**, *53*, 10762-10771.

(64) Engelkemier, J.; Fredrickson, D. C. Chemical Pressure Schemes for the Prediction of Soft Phonon Modes: A Chemist's Guide to the Vibrations of Solid State Materials, *Chem. Mater.* **2016**, *28*, 3171-3183.

(65) The kinetic energy density output by ABINIT output and read into the CP package is in positive definite form.

(66) Martin, R. M. *Electronic Structure: Basic Theory and Practical Methods*; 1st pbk. ed.; Cambridge University Press: Cambridge, UK ; New York, 2008.

(67) Engelkemier, J.; Berns, V. M.; Fredrickson, D. C. First-Principles Elucidation of Atomic Size Effects Using DFT-Chemical Pressure Analysis: Origins of Ca$_{36}$Sn$_{23}$'s Long-Period Superstructure, *J. Chem. Theory Comput.* **2013**, *9*, 3170-3180.

(68) Otero-de-la-Roza, A.; Luaña, V.; Flórex, M. Chapter 1, In *An Introduction to High Pressure Science and Technology*; Recio, J. M., Menéndez, J. M., Otero-de-la-Roza, A., Eds.; CRC Press: Boca Raton, Florida, 2015.

(69) Gonze, X.; Amadon, B.; Anglade, P.-M.; Beuken, J.-M.; Bottin, F.; Boulanger, P.; Bruneval, F.; Caliste, D.; Caracas, R.; Côté, M.; Deutsch, T.; Genovese, L.; Ghosez, P.; Giantomassi, M.; Goedecker, S.; Hamann, D. R.; Hermet, P.; Jollet, F.; Jomard, G.; Leroux, S.; Mancini, M.; Mazevet, S.; Oliveira, M. J. T.; Onida, G.; Pouillon, Y.; Rangel, T.; Rignanese, G.-M.; Sangalli, D.; Shaltaf, R.; Torrent, M.; Verstraete, M. J.; Zerah, G.; Zwanziger, J. W. ABINIT: First-principles Approach to Material and Nanosystem Properties, *Comput. Phys. Commun.* **2009**, *180*, 2582-2615.

(70) Gonze, X.; Rignanese, G.-m.; Verstraete, M.; Beuken, J.-m.; Pouillon, Y.; Caracas, R.; Raty, J.-y.; Olevano, V.; Bruneval, F.; Reining, L.; Godby, R.; Onida, G.; Hamann, D. R.; Allan, D. C. A Brief Introduction to the ABINIT Software Package, *Z. Kristallogr.* **2005**, *220*, 558-562.

(71) Goedecker, S.; Teter, M.; Hutter, J. Separable Dual-space Gaussian Pseudopotentials, *Phys. Rev. B* **1996**, *54*, 1703-1710.

(72) Hartwigsen, C.; Goedecker, S.; Hutter, J. Relativistic Separable Dual-space Gaussian Pseudopotentials from H to Rn, *Phys. Rev. B* **1998**, *58*, 3641-3662.

(73) Fletcher, R. A New Approach to Variable Metric Algorithms, *Comput. J.* **1970**, *13*, 317-322.

10

(74) Monkhorst, H.; Pack, J. Special Points for Brillouin-zone Integrations, *Phys. Rev. B* **1976**, *13*, 5188-5192.

(75) Berns, V. M.; Engelkemier, J.; Guo, Y.; Kilduff, B. J.; Fredrickson, D. C. Progress in Visualizing Atomic Size Effects with DFT-Chemical Pressure Analysis: From Isolated Atoms to Trends in AB_5 Intermetallics, *J. Chem. Theory Comput.* **2014**, *10*, 3380-3392.

(76) Momma, K.; Izumi, F. VESTA 3 for Three-dimensional Visualization of Crystal, Volumetric and Morphology data, *J. Appl. Crystallogr.* **2011**, *44*, 1272-1276.

(77) Burdett, J. K. *Chemical Bonds: A Dialog*; Wiley: Chichester ; New York, 1997.

(78) Baird, N. C. The Chemical Bond Revisited, *J. Chem. Educ.* **1986**, *63*, 660.

(79) Trucano, P.; Chen, R. Structure of graphite by neutron diffraction, *Nature* **1975**, *258*, 136-137.

(80) Klimeš, J.; Michaelides, A. Perspective: Advances and Challenges in Treating van der Waals Dispersion Forces in Density Functional Theory, *J. Chem. Phys.* **2012**, *137*, 120901.

(81) Birowska, M.; Milowska, K.; Majewski, J. Van der Waals density functionals for graphene layers and graphite, *Acta Phys. Pol., A* **2011**, *120*, 845-848.

(82) Wang, Y.; Scheerschmidt, K.; Gösele, U. Theoretical investigations of bond properties in graphite and graphitic silicon, *Phys. Rev. B* **2000**, *61*, 12864-12870.

(83) Sutter, K.; Aucar, G. A.; Autschbach, J. Analysis of Proton NMR in Hydrogen Bonds in Terms of Lone-Pair and Bond Orbital Contributions, *Chem. Eur. J.* **2015**, *21*, 18138-18155.

(84) Grabowski, S. J. What Is the Covalency of Hydrogen Bonding?, *Chem. Rev.* **2011**, *111*, 2597-2625.

(85) Steiner, T. The Hydrogen Bond in the Solid State, *Angew. Chem. Int. Ed.* **2002**, *41*, 48-76.

(86) Silvi, B.; Ratajczak, H. Hydrogen Bonding and Delocalization in the ELF Analysis Approach, *PCCP* **2016**, *18*, 27442-27449.

(87) Weinhold, F.; Klein, R. A. Anti-Electrostatic Hydrogen Bonds, *Angew. Chem. Int. Ed.* **2014**, *53*, 11214-11217.

(88) Müller, U. *Inorganic Structural Chemistry*; 2nd ed.; Wiley: Chichester, England; Hoboken, NJ, 2007.

1
2
3
4
5
6
7
8
9
10
11
12
13
14
15
16
17
18
19
20
21
22
23
24
25
26
27
28
29
30
31
32
33
34
35
36
37
38
39
40
41
42
43
44
45
46
47
48
49
50
51
52
53
54
55
56
57
58
59
60

11

For Table of Contents Use Only

Bonding viewed through chemical pressure maps

Ionic

Metallic

Covalent